

## Research Article

# Simulations of a Single-Phase Flow in a Compound Parabolic Concentrator Reactor

Tzayam Pérez <sup>1</sup> and José L. Nava<sup>2</sup>

<sup>1</sup>Departamento de Ing. Química, Noria Alta, Universidad de Guanajuato, 36050 Guanajuato, GTO, Mexico

<sup>2</sup>Departamento de Ingeniería Geomática e Hidráulica, Av. Juárez 77, Zona Centro, Universidad de Guanajuato, 36000 Guanajuato, GTO, Mexico

Correspondence should be addressed to Tzayam Pérez; [t.perezsegura@ugto.mx](mailto:t.perezsegura@ugto.mx)

Received 21 May 2018; Accepted 17 July 2018; Published 19 August 2018

Academic Editor: Leonardo Palmisano

Copyright © 2018 Tzayam Pérez and José L. Nava. This is an open access article distributed under the Creative Commons Attribution License, which permits unrestricted use, distribution, and reproduction in any medium, provided the original work is properly cited.

This paper deals with the analysis and interpretation of flow visualization and residence time distribution (RTD) in a compound parabolic concentrator (CPC) reactor using computational fluid dynamics (CFD). CFD was calculated under turbulent flow conditions solving the Reynolds averaged Navier–Stokes (RANS) equation expressed in terms of turbulent viscosity and the standard  $k-\epsilon$  turbulent model in 3D. A 3D diffusion-convection model was implemented in the CPC reactor to determine the RTD. The fluid flow visualization and RTD were validated with experimental results. The CFD showed that the magnitude of the velocity field remains almost uniform in most of the bulk reactor, although near and inside the 90° connectors and the union segments, the velocity presented low- and high-speed zones. Comparisons of theoretical and experimental RTD curves showed that the  $k-\epsilon$  model is appropriate to simulate the nonideal flow inside the CPC reactor under turbulent flow conditions.

## 1. Introduction

Compound parabolic concentrator (CPC) reactors have been widely employed in UV light processes of disinfection and water treatment [1], such as photo-Fenton processes [2–5], TiO<sub>2</sub> photocatalytic processes [6–9], or direct irradiation processes [10]. One advantage of this technology is that the source of UV light could be taken from the sun, decreasing operational cost.

Several works show the efficiency of this technology in terms of pollutant concentration decay, during photo-Fenton or solar photoelectro-Fenton water treatment process [2–5, 11]. However, CPC studies that describe its performance from a chemical engineering standpoint are scarce. Among these, the nonideal flow analysis distinguishes, because it allows understanding the bulk reactor behavior and thereby to propose more efficient designs [12].

Most of the homogeneous (photo-Fenton) and heterogeneous (TiO<sub>2</sub> photocatalytic) reactions that take place inside the CPC are performed under turbulent flow conditions to

guarantee complete mixing conditions and an efficient mass transfer. The CPC is a coil-type tubular reactor, and one way to experimentally characterize the hydrodynamics inside it is through residence time distribution (RTD) analysis [13–16] or by flow visualization technique [17–20]. Benhabiles et al. [21] developed an experimental RTD study in a five-tube CPC reactor; these authors estimated Péclet numbers (Pe) and axial dispersion coefficients ( $D_a$ ) with the analytical solution of the axial dispersion model at different volumetric flows. They found that for small values of Pe, the flow presents back mixing and dispersion in the radial direction.

The mathematical models can consider that the flow mixing occurs in the axial coordinate [22–25] and that the flow is completely mixed as the plug-flow model [24, 25]. In practice, flow behavior deviates from these owing to non-uniform velocity profile originated by turbulent diffusivity, by short circuiting, by passing and channeling of fluid, and by the presence of stagnant regions of fluid within the reactor. The above deviations can be determined by the diffusion-convection model, although these are scarcely

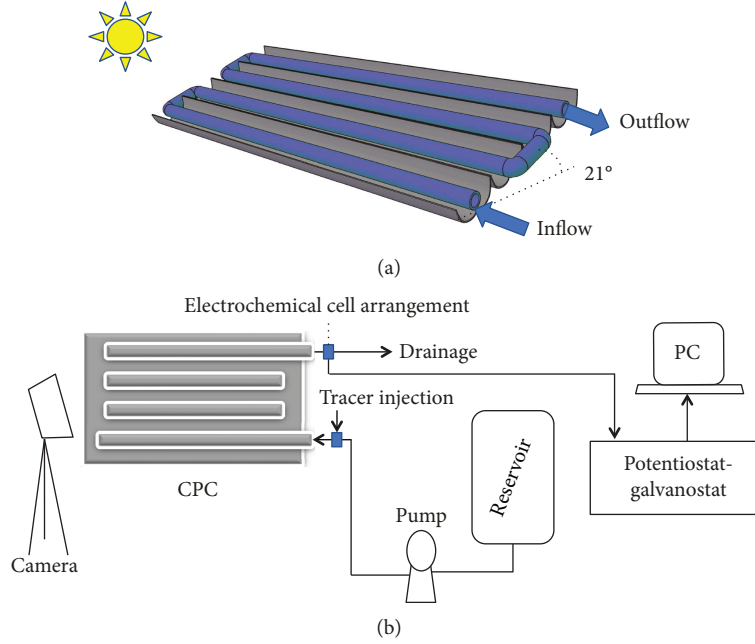


FIGURE 1: (a) Scheme of the CPC reactor. (b) Scheme of the system performed to carry out the experimental RTD studies and the flow visualizations.

modelled. A model for the CPC geometry must include the inclination of the reactor (see Figure 1(a)) owing to it may cause noncomplete mixing conditions.

This paper deals with the analysis and interpretation of flow visualization and RTD in a CPC reactor using CFD in 3D. CFD was calculated under turbulent flow conditions solving the Reynolds averaged Navier–Stokes (RANS) equations expressed in terms of turbulent viscosity and the standard  $k$ – $\varepsilon$  turbulent model. Theoretical RTD curves were compared with experimental RTD data in order to validate the proposed model. Moreover, experimental and theoretical nonideal flow visualization was also performed.

## 2. Description of the CPC Reactor

Figure 1(a) shows a scheme of the CPC reactor which was used as a basis for the computational geometry in order to establish the simulation domain. It consists of 4 acrylic tubes of 90.5 cm length and 1.9 cm inner diameter connected with PVC tube segments and 90° PVC connections of 2.54 cm inner diameter. The parabolic reflectors are made of aluminum with a 180° acceptance angle and a concentration ratio of 1. The system has 1400 cm<sup>3</sup> of capacity and an inclination of 21° from the ground corresponding to the latitude of Guanajuato state, in central Mexico.

## 3. Formulation of the Numerical Simulation

Simulations in 3D of turbulent flow and a tracer inside the reactor were carried out. Figure 2(a) shows the simulation domain, and it was considered as “zigzag” pipes of constant diameter equal to 1.9 cm. The wall roughness was assumed to have a negligible effect. Table 1 shows the parameters for the simulations.

**3.1. Turbulent Flow.** Under turbulent flow conditions, the equations of the model for an incompressible fluid (water) can be stated as follows. The Reynolds averaged Navier–Stokes and the continuity equations are

$$(\rho \mathbf{u} \cdot \nabla) \mathbf{u} = -\nabla P + \nabla \cdot (\mu + \mu_T) (\nabla \mathbf{u} + (\nabla \mathbf{u})^T), \quad (1)$$

$$\nabla \cdot (\rho \mathbf{u}) = 0, \quad (2)$$

where  $\mathbf{u}$  is the velocity vector,  $P$  is the pressure,  $\mu$  is the dynamic viscosity, and  $\rho$  is the fluid density, and the so-called Reynolds stresses can be expressed in terms of a turbulent viscosity  $\mu_T$ , according to the standard  $k$ – $\varepsilon$  turbulence model

$$\begin{aligned} \mu_T &= \rho C_\mu \frac{k^2}{\varepsilon}, \\ \rho(\mathbf{u} \cdot \nabla) k &= \nabla \cdot \left[ \left( \mu + \frac{\mu_T}{\sigma_k} \right) \nabla k \right] + P_k - \rho \varepsilon, \\ \rho(\mathbf{u} \cdot \nabla) \varepsilon &= \nabla \cdot \left[ \left( \mu + \frac{\mu_T}{\sigma_\varepsilon} \right) \nabla \varepsilon \right] + C_{e1} \frac{\varepsilon}{k} P_k - C_{e2} \rho \frac{\varepsilon^2}{k}, \end{aligned} \quad (3)$$

where  $\kappa$  is the turbulent kinetic energy,  $\varepsilon$  is the turbulent energy dissipation rate,  $P_k$  is the energy production term ( $P_k = \mu_T [\nabla \mathbf{u} : (\nabla \mathbf{u} + (\nabla \mathbf{u})^T)]$ ), and  $C_\mu$  (0.09),  $C_{e1}$  (1.44),  $C_{e2}$  (1.92),  $\sigma_k$  (1), and  $\sigma_\varepsilon$  (1.3) are dimensionless constant values that are obtained by data fitting for a wide range of turbulent flows [26–28].

This model is applicable at high Reynolds numbers; for this reason, the near-wall regions, where the velocity is relative to the wall, decrease quickly and these regions are inaccessible by this model. To solve this problem, wall functions

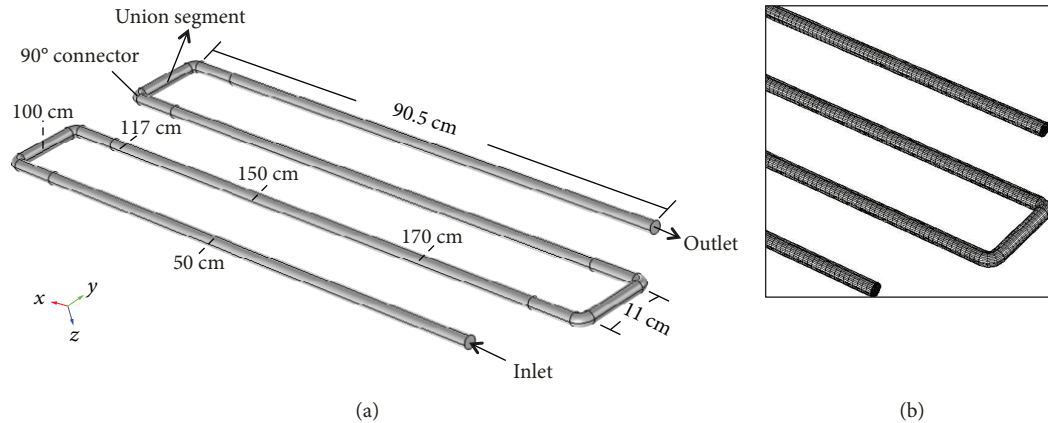


FIGURE 2: (a) Simulation domain established to implement the tracer simulation. The marked distances ( $L = 50$  cm,  $L = 100$  cm,  $L = 117$  cm,  $L = 150$  cm, and  $L = 170$  cm) represent the regions where velocity profiles were taken at  $z = 0$  cm in the center of the tube. (b) Inset of the mesh employed in the simulations.

TABLE 1: Parameters used in the numerical simulation at 293 K.

Initial concentration of $\text{Cu}^{2+}$ , $c_0$ (mol·cm <sup>-3</sup> )	0.05
Dynamic viscosity of water, $\mu$ (gr·cm <sup>-1</sup> ·s <sup>-1</sup> )	0.01
Diffusion coefficient of $\text{Cu}^{2+}$ , $D$ (cm <sup>2</sup> ·s <sup>-1</sup> )	$5 \times 10^{-4}$

based on a universal velocity distribution are usually required. In a turbulent layer, these functions are described by the following equation [26–28]:

$$u^+ = 2.5 \ln y^+ + 5.5, \quad (4)$$

where  $u^+$  is the normalized velocity component inside the logarithmic boundary layer and  $y^+$  is the dimensionless distance from the wall,  $y^+ = \rho u_\tau y / \mu$ , where  $u_\tau$  is the friction velocity,  $u_\tau = C_\mu^{1/4} \sqrt{k}$ , and  $y$  is the thickness from the wall [26–28].

To solve (1), (2), and (3), the corresponding boundary conditions are as follows [26]:

- (1) A normal inflow velocity at the inlet,  $\mathbf{u} = -\mathbf{n}U_0$ ; where  $\mathbf{n}$  is the unit normal vector; in this work, the approximation for the inlet values of  $k_0$  and  $\varepsilon_0$  was obtained from the turbulent intensity  $I_T$  and the turbulent length scale  $L_T$ , by means of the following simple assumed forms:  $k_0 = 3/2(U_0 I_T)^2$  and  $\varepsilon_0 = C_\mu^{3/4} k^{3/2} / L_T$ , where  $I_T$  and  $L_T$  were fixed at 0.05 and 0.0665 cm, respectively [27]. The turbulent intensity for fully turbulent flows has dimensionless values between 0.05 and 0.1. The turbulent length scale can be determined in pipes as a function of the radius by means of  $L_T = 0.07r$ , where  $r$  in this work is the inlet radius of 0.95 cm.
- (2) A normal stress equal to a pressure at the outlet,  $[-P + ((\mu + \mu_T)(\nabla \mathbf{u} + (\nabla \mathbf{u})^T))] \mathbf{n} = -\mathbf{n}P_0$ , with  $\nabla \varepsilon \cdot \mathbf{n} = 0$  and  $\nabla k \cdot \mathbf{n} = 0$ . This last equation expresses that the turbulent characteristic of whatever is outside the computational domain is guided by the flow

inside the computational domain. Such an assumption is physically reasonable as long as relatively small amounts of fluid enter the system [29].

- (3) A velocity  $u^+$  given by (4) at a distance  $y^+$  from a solid surface, for all other boundaries.

After verifying the solution at different values of  $y^+$  and step sizes, the value of  $y^+$  was fixed at 11.1. This value is in the fully turbulent region ( $5 < y^+ < 30$ ), where the turbulent stresses and fluxes are more important. The corresponding values of  $y$  and  $u_\tau$  are  $60 \mu\text{m}$  and  $0.31 \text{ cm}\cdot\text{s}^{-1}$ , respectively. Equations (1), (2), and (3) were solved numerically in stationary regime in 3D through finite elements by using the commercial software COMSOL Multiphysics® (4.4) at different inflow velocities,  $U_0$ :  $17.6 \text{ cm}\cdot\text{s}^{-1}$  ( $\text{Re} = 3344$ ),  $22.2 \text{ cm}\cdot\text{s}^{-1}$  ( $\text{Re} = 4218$ ), and  $24.4 \text{ cm}\cdot\text{s}^{-1}$  ( $\text{Re} = 4636$ ). A simulation domain of 41,500 mesh elements was considered (Figure 2(b)). The numerical accuracy of the magnitude of the local velocity vectors was tested by enlarging and diminishing the size of the tetrahedral elements by a factor of 2 and by verifying that the solution of the magnitude of the local velocity vectors did not show significant differences as the convergence criterion was changed to below  $10^{-5}$ . The simulation run times were typically from 30 to 45 minutes depending on the flow rate. A computer with 2 intel® Xeon 2.3 GHz processors, 96 GB of RAM, and 64 bits of operative system was employed.

**3.2. Tracer Simulation.** The time-dependent behavior of a tracer inside the reactor could be described by the general form of the diffusion-convection equation [30]

$$\frac{\partial c}{\partial t} = D \nabla^2 c - \mathbf{u} \cdot \nabla c, \quad (5)$$

where  $c$  is the concentration of the tracer,  $t$  is the time,  $D$  is the diffusion coefficient, and  $\mathbf{u}$  is the velocity vector obtained by the solution of (1).

It is important to mention that in some cases, mass transport models are involved with turbulent flow conditions, the

term of turbulent diffusivity that appears in (5). This term is associated to jet flows, eddies, and local flow deviations caused by the inherent turbulent flow inside the system [31, 32]. Worthy of mentioning, we performed several simulations including the turbulent diffusivity coefficient (not shown herein) in order to develop a more rigorous model. However, when this term was included, the theoretical results did not fit with the experimental RTD studies. The explanation of the above behavior is discussed in the analysis of results and discussion in Section 5.

In order to simulate the tracer injection in an instant of time, a Gaussian pulse function was employed [33]

$$y(t) = \frac{1}{\sigma\sqrt{2\pi}} e^{-(t-t_0)^2/2\sigma^2}, \quad (6)$$

where  $\sigma$  is the standard deviation and  $t$  is the time which was fixed in an interval of time from 0 to 6 seconds. After several trials and verifying the solution, the standard deviation was fixed at 2 s. In this paper, the diffusion coefficient was fixed at  $D = 5 \times 10^{-4} \text{ cm}^2 \cdot \text{s}^{-1}$ .

In order to solve (5) and considering complete mixing conditions before the inlet and after the outlet of the reactor (Figure 2(a)), the boundary and the initial conditions established are as follows:

- (i) Before tracer injection inside the reactor at  $t=0$ ,  $c(x, y, z, t) = 0$
- (ii) An initial concentration at the inlet,  $c = c_0 y(t)/y(t=0)$
- (iii) Cero flux at the outlet and at the walls,  $D\nabla c = 0$

Equation (5) was solved numerically in 3D through finite elements by using the commercial software COMSOL Multiphysics (4.4) at different inflow velocities: 17.6, 22.2, and  $24.4 \text{ cm} \cdot \text{s}^{-1}$ . Equation (5) is in transient state; therefore, it needs an interval of time to be solved, which was established from  $t=0 \text{ s}$  to  $t=140 \text{ s}$  at 0.1 s of step size. A simulation domain of 41,500 mesh elements was considered. The simulation run times were typically from 20 to 30 minutes depending on the flow rate.

After solving (5), theoretical RTD curves and computational animations were performed in order to compare with experimental RTD curves and flow visualizations at different inflow velocities.

## 4. Experimental Details

The experimental flow visualization and RTD were performed in order to compare the theoretically obtained CFD and RTD results. Experimental tracer tests were filmed by a high-resolution camera and those were compared with computational tracer animations.

**4.1. Flow Visualization.** In order to visualize experimental flow patterns inside the CPC reactor, 5 mL of colored tracer (Blue 1 at a concentration of  $5 \text{ g} \cdot \text{L}^{-1}$ ) was injected few centimeters before the CPC inlet and filmed (Figure 1(b)). It is important to mention that the density of the tracer solution

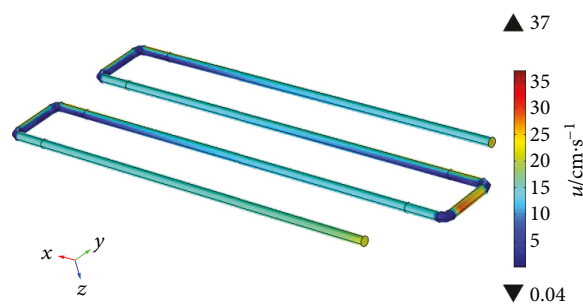


FIGURE 3: Velocity magnitude field plot inside the CPC reactor for an inflow velocity of  $22.2 \text{ cm} \cdot \text{s}^{-1}$ .

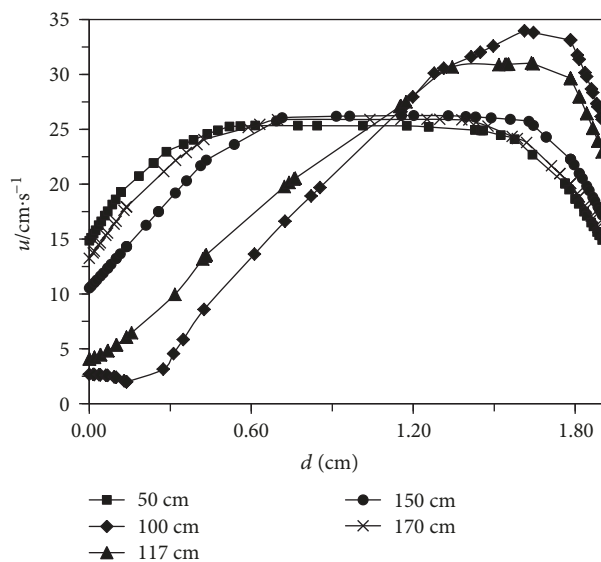


FIGURE 4: Velocity magnitude profiles inside the CPC reactor as a function of the diameter in the center of the tube at  $z=0 \text{ cm}$ . These profiles were taken at different distances,  $L=50 \text{ cm}$  (black square),  $L=100 \text{ cm}$  (black diamond),  $L=117 \text{ cm}$  (black triangle),  $L=150 \text{ cm}$  (black circle), and  $L=170 \text{ cm}$  ( $\times$ ) from the inlet of the reactor for an inflow velocity of  $22.2 \text{ cm} \cdot \text{s}^{-1}$ .

does not affect the flow pattern inside the reactor. Moreover, the tracer volume is significantly smaller than the volume of the reactor (1400 mL). A 29-frames-per-second and  $1920 \times 1080$ -pixel-resolution camera was used. The tracer tests were performed at different inflow velocities of 17.6, 22.2, and  $24.4 \text{ cm} \cdot \text{s}^{-1}$ .

**4.2. RTD Studies.** To determine the mixing flow pattern in the liquid phase, the stimulus response technique was employed. 5 mL of 0.05 M copper sulfate was injected as tracer at the inlet of the CPC and the cupric ions were detected at the exit (Figure 1(b)). The measurement of Cu(II) was carried out employing a typical two-electrode cell arrangement using two copper wires as electrodes; the cupric ions were quantified by typical transient current at a holding cell potential of  $-1.9 \text{ V}$ . The current response was recorded every 0.5-seconds by a potentiostat-galvanostat model SP-150 from BioLogic™ with EC-Lab® software. It is important to mention

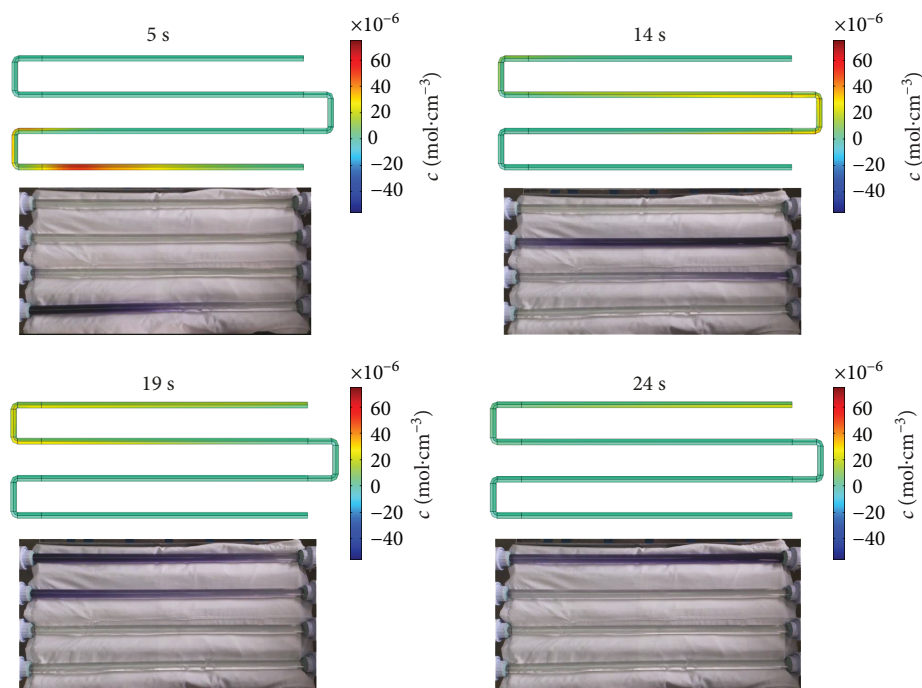


FIGURE 5: Comparisons of different pictures taken from the flow visualizations and the computational animations at different times of 5, 14, 19, and 24 seconds for an inflow velocity of  $22.2 \text{ cm}\cdot\text{s}^{-1}$ .

that at such cell potential of  $-1.9 \text{ V}$ , a limiting current of copper deposition governs the cathodic process ensuring that the response only depends on the cupric ion concentration.

For the nonideal flow, elements of fluid can take different routes throughout the CPC reactor, spending different periods of time inside the reactor. The RTD curve,  $E(t)$ , describes the distribution of these periods of time for the stream of fluid leaving the CPC, (7). The  $E(t)$  function is normalized and the area under the curve reaches a value of 1, according to (8) [12]

$$\int_0^{\infty} E(t) dt = 1, \quad (7)$$

$$E(t) = \frac{I(t)}{\int_0^{\infty} I(t) dt}, \quad (8)$$

where  $I(t)$  is the time-dependent current response. RTD studies were carried out at different inflow velocities of  $17.6$ ,  $22.2$  and  $24.4 \text{ cm}\cdot\text{s}^{-1}$ .

## 5. Analysis of Results and Discussion

**5.1. Turbulent Flow.** Figure 3 shows a domain velocity field plot for a characteristic inflow velocity of  $22.2 \text{ cm}\cdot\text{s}^{-1}$  inside the CPC reactor. Here, it could be observed that the velocity field remains almost uniform in most of the bulk reactor. However, near and inside the  $90^\circ$  connectors and the union segments, the velocity field presents low- and high-velocity zones due to the inherent CPC geometry, showing that the CPC cannot be considered as an ideal plug flow reactor.

Identical patterns (not shown herein) were obtained for the other inflow velocities,  $17.6$  and  $24.4 \text{ cm}\cdot\text{s}^{-1}$ .

Figure 4 shows velocity profiles as a function of the tube diameter for a characteristic inflow velocity of  $22.2 \text{ cm}\cdot\text{s}^{-1}$ . These curves were constructed in order to describe the hydrodynamic behavior of Figure 3. The velocity profiles inside the inner diameter were constructed at different distances from the CPC inlet as shown in Figure 2(a). The profile constructed at distance of  $50 \text{ cm}$  develops an ideal turbulent profile with a maximum of around  $25 \text{ cm}\cdot\text{s}^{-1}$  and a minimum of around  $15 \text{ cm}\cdot\text{s}^{-1}$  and a plug flow region of around  $0.4 \leq d \leq 1.6 \text{ cm}$ . The velocity profile for the union segment at a distance of  $100 \text{ cm}$  shows the flow deviations generated by the  $90^\circ$  connector. In this profile, it could be observed that the union segment presents low velocity values of around  $0 \leq d \leq 0.13 \text{ cm}$  with a minimum value of  $2 \text{ cm}\cdot\text{s}^{-1}$ ; then, the velocity increases until it reaches a maximum of  $34 \text{ cm}\cdot\text{s}^{-1}$  at  $d = 1.6 \text{ cm}$ . After, the velocity decreases until  $26 \text{ cm}\cdot\text{s}^{-1}$  at  $d = 1.9 \text{ cm}$ . The above behavior is very similar for the profile at a distance of  $117 \text{ cm}$ ; here, it could be seen that this behavior is less pronounced that the profile performed at  $100 \text{ cm}$ , which means that the flow deviations attenuate away from the  $90^\circ$  connection as can be observed at distances of  $150$  and  $170 \text{ cm}$ . The behavior described in the profiles repeats in every lap of the CPC confirming the need to analyze the RTD. Similar plots not shown herein were obtained for the other inflow velocities at  $17.6$  and  $24.4 \text{ cm}\cdot\text{s}^{-1}$ , obtaining the same pattern.

From the analysis of Figures 3 and 4, it could be confirming the convenience of using a mass transport model without the turbulent diffusion coefficient, described in Section 3.2. The above is because the system does not generate significant

turbulent flow deviations such as eddies or jet flows, as it can be observed in Figure 3; this behavior confirms the omission of the turbulent diffusion coefficient of (5). Moreover, the velocity profiles develop a pseudoplug flow behavior in almost all regions inside the reactor (Figure 4); this last showed that the system is appropriate to develop a well homogenous environment to carry out the photoreactions inside the system. The above was proved in the analysis of results and discussion of the flow visualization and RTD described below. Nevertheless, a deeper analysis with different photocatalytic reactions is needed to support this statement. This later was beyond the scope of this paper.

**5.2. Flow Visualization.** Figure 5 shows comparisons of the experimental flow visualization and the tracer simulation at different times for the characteristic inflow velocity of  $22.2 \text{ cm}\cdot\text{s}^{-1}$ . Here, it could be observed qualitatively that the tracer simulation agrees with the experimental visualization technique, because the tracer follows the same flow patterns at the same instants of time. For the time of 5 seconds, the tracer is completely mixed before entering the  $90^\circ$  connection. After the first union segment, at the time of 14 seconds, the tracer presents an elongation generated by the  $90^\circ$  connection. This elongation is more marked passing the third and fourth union segments at the time of 19 and 24 seconds, respectively; therefore, it agrees with those discussed in Figures 3 and 4; the  $90^\circ$  connections generate slow-velocity zones and flow deviations. Similar experimental flow visualization and the tracer simulation were obtained for  $17.6$  and  $24.4 \text{ cm}\cdot\text{s}^{-1}$  (not shown), obtaining the same pattern to that obtained at  $22.2 \text{ cm}\cdot\text{s}^{-1}$ .

**5.3. RTD.** Figure 6 presents comparisons of theoretical and experimental RTD curves for the different inflow velocities as a function of the dimensionless residence time ( $t/\tau$ ), where  $\tau$  is the spatial residence time given by the ratio between the length of the CPC and the inflow velocity ( $=L/U_0$ ). This figure shows close agreement between experiments and simulations (error < 5%). Worthy of mentioning, the most fluid elements leave the system around the expected residence time ( $t/\tau=1$ ). For such cases, the residence time is about 24 s and the dispersion of the tracer in the pipe is dominated by the convective transport, where the turbulent flow predominates ( $Re > 3000$ ).

From the analysis carried out here, a CPC reactor develops nonideal flow distribution in the  $90^\circ$  connections, which could influence the efficiency of this technology to be employed in UVA light processes of water treatment, such as photo-Fenton process. This later should serve as a starting point for future research.

## 6. Conclusions

This work presented a way to analyze the hydrodynamic behavior inside a CPC reactor. A 3D diffusion-convection model was implemented considering that the flow is not completely mixed inside the CPC reactor. A single-phase flow analysis was performed solving the RANS equations with the standard  $k-\epsilon$  turbulent model, for  $Re > 3000$ .

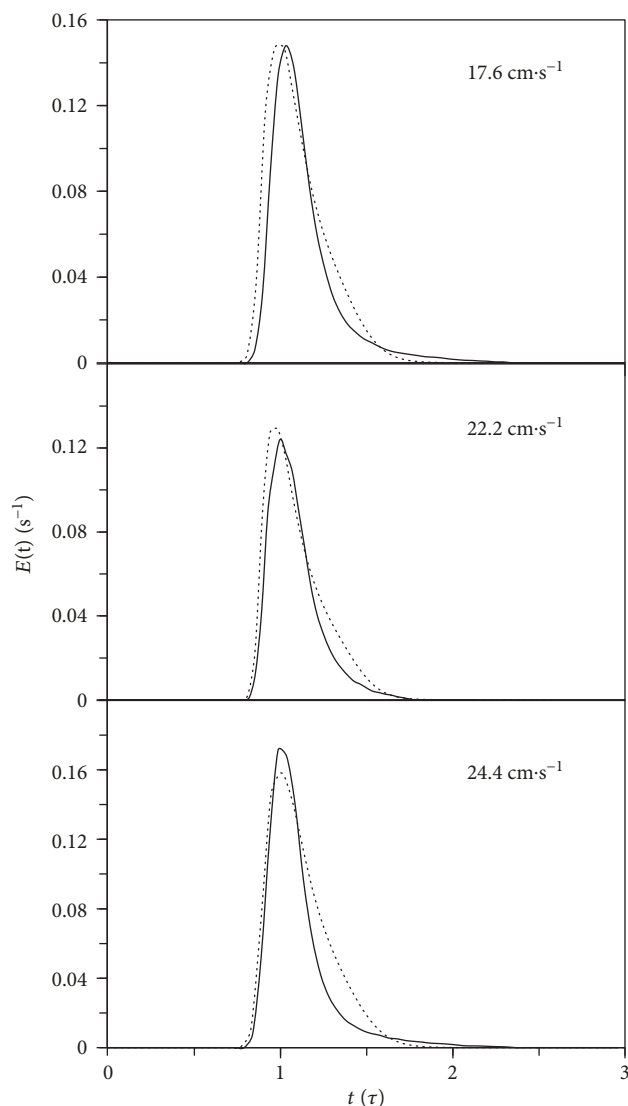


FIGURE 6: Comparisons of experimental (solid line) and theoretical (dot line) RTD curves as a function of the dimensionless residence time at different inflow velocities showed inside the figure.

The analysis of the turbulent flow simulations showed that near and inside the  $90^\circ$  connectors and the union segments, the reactor presents low- and high-velocity zones owing to the inherent CPC geometry, showing that the CPC cannot be considered as an ideal plug flow reactor. An appropriate CPC reactor design must consider the flow behavior deviations caused by the perpendicular union segments of the CPC. Then, other connection angles should be tested to improve the hydrodynamics within the “zigzag tubes” and, consequently, to improve the mixing conditions in the photoreactor.

The comparison of flow visualization studies and the computational animations showed good agreement for the inflow velocities of  $17.6$ ,  $22.2$ , and  $24.4 \text{ cm}\cdot\text{s}^{-1}$ . Excellent agreement between theoretical and experimental RTD curves was obtained. This later shows the robustness of the proposed model, envisaging a future application in photo-Fenton-like processes for water treatment. The mathematical

model proposed here can be helpful for scaling up the CPC photoreactor, where photoreactions should be adapted, although a deeper analysis with different photocatalytic reactions is needed to support this assertion.

## Data Availability

No external data were used to support this study. All data reported here could be reproduced implementing the methodology described in this work.

## Conflicts of Interest

The authors declare that there is no conflict of interest regarding the publication of this paper.

## Acknowledgments

The authors thank the University of Guanajuato for funding through Project no. 100/2018 and Project PRODEP no. UGTO-PTC-615.

## References

- [1] D. Spasiano, R. Marotta, S. Malato, P. Fernandez-Ibañez, and I. Di Somma, "Solar photocatalysis: materials, reactors, some commercial, and pre-industrialized applications. A comprehensive approach," *Applied Catalysis B: Environmental*, vol. 170-171, pp. 90-123, 2015.
- [2] T. Pérez, S. Garcia-Segura, A. El-Ghenemy, J. L. Nava, and E. Brillas, "Solar photoelectro-Fenton degradation of the antibiotic metronidazole using a flow plant with a Pt/air-diffusion cell and a CPC photoreactor," *Electrochimica Acta*, vol. 165, pp. 173-181, 2015.
- [3] R. Salazar, E. Brillas, and I. Sirés, "Finding the best  $\text{Fe}^{2+}/\text{Cu}^{2+}$  combination for the solar photoelectro-Fenton treatment of simulated wastewater containing the industrial textile dye Disperse Blue 3," *Applied Catalysis B: Environmental*, vol. 115-116, pp. 107-116, 2012.
- [4] T. Perez, I. Sires, E. Brillas, and J. L. Nava, "Solar photoelectro-Fenton flow plant modeling for the degradation of the antibiotic erythromycin in sulfate medium," *Electrochimica Acta*, vol. 228, pp. 45-56, 2017.
- [5] G. Coria, T. Pérez, I. Sirés, E. Brillas, and J. L. Nava, "Abatement of the antibiotic levofloxacin in a solar photoelectro-Fenton flow plant: modeling the dissolved organic carbon concentration-time relationship," *Chemosphere*, vol. 198, pp. 174-181, 2018.
- [6] I. García-Fernández, I. Fernández-Calderero, M. I. Polo-López, and P. Fernández-Ibañez, "Disinfection of urban effluents using solar  $\text{TiO}_2$  photocatalysis: a study of significance of dissolved oxygen, temperature, type of microorganism and water matrix," *Catalysis Today*, vol. 240, no. A, pp. 30-38, 2015.
- [7] S. García-Segura and E. Brillas, "Applied photoelectrocatalysis on the degradation of organic pollutants in wastewaters," *Journal of Photochemistry and Photobiology C: Photochemistry Reviews*, vol. 31, pp. 1-35, 2017.
- [8] D. M. El-Mekkawi, N. Nady, N. A. Abdelwahab, W. A. A. Mohamed, and M. S. A. Abdel-Mottaleb, "Flexible bench-scale recirculating flow CPC photoreactor for solar photocatalytic degradation of methylene blue using removable  $\text{TiO}_2$  immobilized on PET sheets," *International Journal of Photoenergy*, vol. 2016, Article ID 9270492, 9 pages, 2016.
- [9] E. M. Saggiaro, A. S. Oliveira, T. Pavesi et al., "Solar CPC pilot plant photocatalytic degradation of indigo carmine dye in waters and wastewaters using supported- $\text{TiO}_2$ : influence of Photodegradation parameters," *International Journal of Photoenergy*, vol. 2015, Article ID 656153, 12 pages, 2015.
- [10] J. Ndounla et al., "Relevant impact of irradiance (vs. dose) and evolution of pH and mineral nitrogen compounds during natural water disinfection by photo-Fenton in a solar CPC reactor," *Applied Catalysis B: Environmental*, vol. 148-149, pp. 144-153, 2014.
- [11] S. Garcia-Segura, E. B. Cavalcanti, and E. Brillas, "Mineralization of the antibiotic chloramphenicol by solar photoelectro-Fenton: from stirred tank reactor to solar pre-pilot plant," *Applied Catalysis B: Environmental*, vol. 144, pp. 588-598, 2014.
- [12] H. S. Fogler, *Elements of Chemical Reaction Engineering*, Prentice Hall, New Jersey, USA, 2005.
- [13] P. Ghosh, K. Vahedipour, M. Lin, J. H. Vogel, C. Haynes, and E. von Lieres, "Computational fluid dynamic simulation of axial and radial flow membrane chromatography: mechanisms of non-ideality and validation of the zonal rate model," *Journal of Chromatography A*, vol. 1305, pp. 114-122, 2013.
- [14] F. Jovic, V. Kosar, V. Tomasic, and Z. Gomzi, "Non-ideal flow in an annular photocatalytic reactor," *Chemical Engineering Research and Design*, vol. 90, no. 9, pp. 1297-1306, 2012.
- [15] Q. Li, M. C. Henstridge, C. Batchelor-McAuley, N. S. Lawrence, R. S. Hartshorne, and R. G. Compton, "Glassy carbon tubular electrodes for the reduction of oxygen to hydrogen peroxide," *Physical Chemistry Chemical Physics*, vol. 15, no. 20, pp. 7854-7865, 2013.
- [16] P. Rojahn, V. Hessel, K. D. P. Nigam, and F. Schael, "Applicability of the axial dispersion model to coiled flow inverters containing single liquid phase and segmented liquid-liquid flows," *Chemical Engineering Science*, vol. 182, pp. 77-92, 2018.
- [17] M. Ansari, D. E. Turney, R. Yakobov et al., "Chemical hydrodynamics of a downward microbubble flow for intensification of gas-fed bioreactors," *AIChE Journal*, vol. 64, no. 4, pp. 1399-1411, 2018.
- [18] D. Patel, F. Ein-Mozaffari, and M. Mehrvar, "Using tomography to visualize the continuous-flow mixing of biopolymer solutions inside a stirred tank reactor," *Chemical Engineering Journal*, vol. 239, pp. 257-273, 2014.
- [19] W.-F. Li, K.-J. du, G.-S. Yu, H.-F. Liu, and F.-C. Wang, "Experimental study of flow regimes in three-dimensional confined impinging jets reactor," *AIChE Journal*, vol. 60, no. 8, pp. 3033-3045, 2014.
- [20] G. Wang, Z. Li, M. Yousaf, X. Yang, and M. Ishii, "Experimental study on vertical downward air-water two-phase flow in a large diameter pipe," *International Journal of Heat and Mass Transfer*, vol. 118, pp. 919-930, 2018.
- [21] O. Benhabiles, N. Chekir, and W. Taane, "Determining of the residence time distribution in CPC reactor type," *Energy Procedia*, vol. 18, pp. 368-376, 2012.
- [22] S. A. Martínez-Delgadillo, H. R. Mollinedo P., M. A. Gutiérrez, I. D. Barceló, and J. M. Méndez, "Performance of a tubular electrochemical reactor, operated with different inlets, to remove Cr(VI) from wastewater," *Computers & Chemical Engineering*, vol. 34, no. 4, pp. 491-499, 2010.

- [23] F. F. Rivera, M. R. Cruz-Díaz, E. P. Rivero, and I. González, "Analysis and interpretation of residence time distribution experimental curves in FM01-LC reactor using axial dispersion and plug dispersion exchange models with closed-closed boundary conditions," *Electrochimica Acta*, vol. 56, no. 1, pp. 361–371, 2010.
- [24] A. Safari, J. Safdari, H. Abolghasemi, M. Foroughi, and M. Moghaddam, "Axial mixing and mass transfer investigation in a pulsed packed liquid-liquid extraction column using plug flow and axial dispersion models," *Chemical Engineering Research and Design*, vol. 90, no. 2, pp. 193–200, 2012.
- [25] P. Trinidad, C. Ponce de León, and F. C. Walsh, "The application of flow dispersion models to the FM01-LC laboratory filter-press reactor," *Electrochimica Acta*, vol. 52, no. 2, pp. 604–613, 2006.
- [26] T. Pérez, C. Ponce de León, F. C. Walsh, and J. L. Nava, "Simulation of current distribution along a planar electrode under turbulent flow conditions in a laboratory filter-press flow cell," *Electrochimica Acta*, vol. 154, pp. 352–360, 2015.
- [27] H. K. Versteeg and W. Malalasekera, *An Introduction to Computational Fluid Dynamics: The Finite Volume Method*, Prentice Hall, London, 1995.
- [28] P. S. Bernard and J. M. Wallace, *Turbulent Flow: Analysis, Measurement, and Prediction*, John Wiley & Sons, New Jersey, 2002.
- [29] D. C. Wilcox, *Turbulence Modeling for CFD*, DCW Industries Inc., La Cañada Flintridge, CA, USA, 1998.
- [30] R. B. Bird, W. E. Stewart, and E. N. Lightfoot, *Transport Phenomena*, John Wiley & Sons, New York, 2002.
- [31] M. R. Cruz-Díaz, E. P. Rivero, F. J. Almazán-Ruiz, Á. Torres-Mendoza, and I. González, "Design of a new FM01-LC reactor in parallel plate configuration using numerical simulation and experimental validation with residence time distribution (RTD)," *Chemical Engineering and Processing: Process Intensification*, vol. 85, pp. 145–154, 2014.
- [32] E. P. Rivero, M. R. Cruz-Díaz, F. J. Almazán-Ruiz, and I. González, "Modeling the effect of non-ideal flow pattern on tertiary current distribution in a filter-press-type electrochemical reactor for copper recovery," *Chemical Engineering Research and Design*, vol. 100, pp. 422–433, 2015.
- [33] M. J. Rivera, M. Trujillo, V. Romero-García, J. A. López-Molina, and E. Berjano, "Numerical resolution of the hyperbolic heat equation using smoothed mathematical functions instead of Heaviside and Dirac delta distributions," *International Communications in Heat and Mass Transfer*, vol. 46, pp. 7–12, 2013.



Hindawi

Submit your manuscripts at  
[www.hindawi.com](http://www.hindawi.com)

